Available online at www.sciencedirect.com
ScienceDirect
Journal of Nuclear Materials 373 (2008) 90–93
journal of nuclear materials
www.elsevier.com/locate/jnucmat

Local atomic structure in $(Zr_{1-x}U_x)N$

M. Walter [a,*], J. Somers [a], A. Fernández-Carretero [a], J. Rothe [b]

[a] European Commission, Joint Research Centre, Institute for Transuranium Elements, P.O. Box 2340, D-76125 Karlsruhe, Germany
[b] Forschungszentrum Karlsruhe, Institut für Nukleare Entsorgung (INE), P.O. Box 3640, D-76021 Karlsruhe, Germany

Received 24 October 2006; accepted 7 May 2007

Abstract

$(Zr_{1-x}U_x)N$ solid solutions were prepared for EXAFS measurements by a sol–gel route combined with infiltration and carbothermic reduction. The lattice parameter and the more distant coordination shells (Me_2 and Me_3) around the Zr and U atoms follow the Vegard law. In the first coordination shell, the U–N distance also follows the Vegard law. Though the Zr–N bond distance increases with the lattice expansion caused by increasing U content, it remains constant at 232–235 pm in U-rich $(Zr_{1-x}U_x)N$ ($x > 0.6$). The measurements indicate that U accommodates the lattice contraction with increasing Zr content, whereas Zr is able to expand its Zr–N bond only at lower U content. In the composition range of transmutation fuels, $(Zr_{1-x}U_x)N$ is homogeneous at the local atomic scale.

1. Introduction

The transmutation of minor actinides (MA: Np, Am, Cm) in fast flux reactors or in accelerator driven systems (ADS) is a relatively recent approach to reduce their long–term radiotoxicity. To obtain a high MA transmutation efficiency, UO_2 cannot be used as a support matrix, rather matrices inert to neutron capture should be used. Due to its advantageous physical properties (high thermal conductivity, high melting point), ZrN has been proposed as such an inert matrix [1].

ZrN and actinide mononitrides such as UN and PuN crystallize in the face-centred cubic structure ($Fm\bar{3}m$). Since the lattice parameters are similar (ZrN: 457.45 pm [2], UN: 488.8 pm [3]; PuN: 490.5 pm [4]), ZrN and actinide mononitrides form solid solutions. Complete solubility is reported for ZrN–UN [5] and ZrN–PuN [6,7]. The miscibility seems to be limited in the case of ZrN–ThN [4] and ZrN–AmN [7], and is most likely due to the larger difference in the end member lattice parameters (ThN: 515.5 pm, [4], AmN 499.1 pm, [7]). Generally, the lattice parameter of solid solution compounds obtained by X-ray diffraction is averaged over several unit cells (coherence) and does not reflect the local structure and bonding behaviour of the different atomic constituents. This information (bond length, local disorder, cooperative effects) can be provided by extended X-ray absorption fine structure (EXAFS), which is a direct probe of the atomic environment surrounding the absorbing atom.

EXAFS has been used already to determine the local structure of the actinide solid solutions $(U,Ce)O_2$ [8], $(Th,U)O_2$ [9], $(Th,Pu)O_2$ [9] and (U,La)S [10]. It has been shown that the local structure around the different metals can differ from that of the bulk crystallographic structure determined by X-ray diffraction. This concerns mainly the bond length of the first coordination shell around the metals. In the case of (Zr,U)N – which represents the experimentally most simple (Zr, actinide)N system – no such information is available and thus is addressed in this work. Indeed these investigations form part of a more extensive project to determine structural and thermodynamic properties of such actinide bearing materials and will eventually culminate in irradiation testing of selected candidate materials.

* Corresponding author. Tel.: +49 7247 951 130; fax: +49 7247 951 566.
E-mail address: marcus.walter@ec.europa.eu (M. Walter).

0022-3115/$ - see front matter © 2007 Elsevier B.V. All rights reserved.
doi:10.1016/j.jnucmat.2007.05.027

2. Experimental

2.1. Sample preparation

(Zr,U)N samples were prepared by the sol–gel and the infiltration route [11] combined with subsequent carbothermical reduction of 'carboneous' $(Zr,U)O_2$ spheres. In a first step, porous $ZrO_2 + C$ sol–gel spheres were prepared by gel-supported precipitation. Zirconyl chloride (purity 99.9%, Alfa Aesar) was dissolved in deionised water and a polymer (methocel, Dow Chemicals) was then added to this solution to increase its viscosity. Carbon black (Kropfmühl AG, Hauzenberg, Germany) was added in a slight excess (C/metal ≈ 2.3) to ensure the presence of sufficient carbon for the carbothermic reduction. This suspension was then atomized and the droplets collected in an ammonia bath, where ammonia diffuses into the original droplet and causes precipitation of the hydroxides. The resulting beads were then calcined under an argon atmosphere at 800 °C to give the oxide. For lower values of x (0.04, 0.10, 0.20, 0.25 and 0.40) porous $ZrO_2 + C$ beads were prepared and infiltrated with equivalent amounts of uranyl nitrate (Merck) solution. To remove humidity and nitrate ions from the materials, they were calcined at 800 °C in argon to give $(Zr_{1-x}U_x)O_2 + C$ beads. The samples with $x = 0.6$, 0.75, 0.9, 0.96, and 1.00 were directly prepared via gel-supported precipitation by mixing zirconyl chloride and uranyl nitrate solutions in the desired proportion.

In the second step, the $(Zr,U)O_2 + C$ particles were transformed into the nitride by carbothermic reduction [12]:

$$(Zr_{1-x},U_x)O_2 + C + 1/2N_2 \rightarrow (Zr_{1-x}U_x)N + 2CO$$

This reaction was performed in a Degussa metallic furnace under a flowing nitrogen gas stream at 1600 °C. The reaction time was about 12 h, and was terminated when the CO was no longer present in the exhaust gas. Thus, the carbothermic reaction was considered to be finished and the atmosphere changed to N_2/H_2 (1.2 bar, 8% H_2) for 46 h to remove excess carbon [3]. The cooling down was performed under Ar/H_2 (8% H_2) to prevent formation of sesquinitrides. The N content in the samples was not measured. Nevertheless, the preparation procedure was sufficiently close to that of Holleck et al. [5], to be sure that the Zr rich samples did not become substoichiometric in N. Indeed, the lattice parameters of the samples prepared in this work follow the Vegard law and are in good agreement with the literature values of Holleck [4,5].

2.2. X-ray diffraction and EXAFS measurement

X-ray diffraction patterns of the $(Zr_{1-x}U_x)N$ samples were recorded in Bragg–Brentano mode using a Phillips PW1050/70 goniometer equipped with a Cu Kα X-ray source and a scintillation counter. Only the diffraction peaks of a single $Fm\bar{3}m$ phase were present and no other phases, such as sesquinitrides or oxides, were observed.

For EXAFS measurements the samples were milled and mixed with boron nitride. The EXAFS data at the Zr K-edge and U L_3-edge were recorded at room temperature in transmission mode at the INE–Beamline for actinide research at the Ångströmquelle Karlsruhe, ANKA [13]. Due to the low Zr content in the $(Zr_{1-x}U_x)N$ samples with $x = 0.9$ and 0.96, the Zr–K edge EXAFS data of these samples were measured in fluorescence mode using a five element LEGe solid state detector (Canberra-Eurisys). The double-crystal monochromator (DCM) was equipped with a pair of Ge(422) crystals, energy calibrated against the first derivative XANES spectrum of a Zr foil. The EXAFS oscillations were extracted according to standard procedures (background removal using a polynomial pre-edge fit, normalization, a spline fit for removal of the atomic background, etc.) using the EXAFSPAK [14] software package. The ionization threshold energy, E_0, used to define the origin for calculation of the *chi*(k)-function was set at 18 010 eV for Zr spectra and 17 185 eV for U L_3-edge spectra.

2.3. Evaluation of the calculated backscattering paths

Theoretical phase shifts, $\delta(k)$, and backscattering amplitudes, $F(k)$, were calculated with the FEFF8 code [15] using spherical clusters of $(Zr_{1-x}U_x)N$, with $r = 750$ pm. The atomic positions within the $(Zr_{1-x}U_x)N$ clusters for these calculations were determined assuming a Vegard behaviour and a random metal distribution. The relevant scattering paths determined from these calculations are shown in Fig. 1. From the backscattering atoms in the unit cell, only the single scattering paths of the nearest (N_1) and next-nearest (Me_1) coordination shells are important. The backscattering amplitude of the 8 N atoms at the unit cell

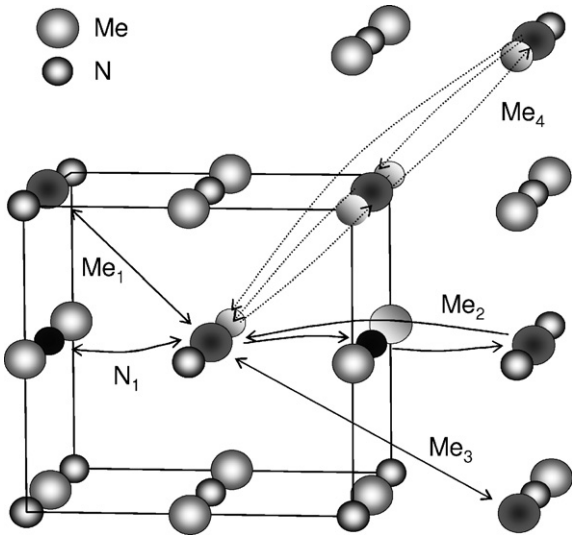

Fig. 1. Crystal structure of MeN (Me: $Zr_{1-x}U_x$)N showing the significant scattering paths: SS N_1 (Me_0–N_1–Me_0), SS Me_1 (Me_0–Me_1–Me_0), MS3 Me_2 (Me_0–N_1–Me_2–Me_0), SS Me_3 (Me_0–Me_3–Me_0), MS3 Me_4 (Me_0–Me_1–Me_4–Me_0) and MS4 Me_4(Me_0–Me_1–Me_4–Me_1–Me_0).

corner is low and not significant, but scattering from three more distant metal coordination shells (Me_2, Me_3, Me_4) must be included. The net Me_2 shell contribution is dominated by the three-legged multiple scattering (MS) path Me_0–N_1–Me_2–Me_0, whereas the single scatting (SS) path and four-legged MS path Me_0–N_1–Me_2–N_1–Me_0 are shifted in phase and cancel each other out. Thus only the three-legged MS path was included for the Me_2 shell. The contribution of the third Me shell (Me_3) is dominated by a SS path. The Me_4 SS path is not of relevance, but the three-legged and four-legged MS paths along Me_0–Me_1–Me_4 are equal in amplitude and both must be included in the fit. For the Me_4 shell, the Zr–U substitution results in four different paths since in the Me_0–Me_1–Me_4 path both Me_1 and Me_4 can be occupied by Zr or U. To reduce the number of variables in the fit, the interatomic distance (R) and the Debye–Waller factor (σ^2) were linked for the Zr and U backscatters. The coordination number (N) of the Me_1 shell was allowed to vary, but the sum of $N(Me_0$–$Zr_1)$ and $N(Me_0$–$U_1)$ was held constant at the crystallographic value of 12. For the more distant Me shells Me_2 and Me_3 a homogenous Zr–U distribution was assumed and the values of N(Zr) and N(U) were set according the bulk sample composition. The amplitude reduction factor was held constant at 1.0 and the shift in threshold energy, ΔE_0, was varied as a global parameter in the fits. All fits were performed in k-space with EXAFSPAK using a k-range of 0.034–0.12 pm^{-1} and 0.032–0.12 pm^{-1} for the Zr K and U L_3-EXAFS, respectively.

3. Results

The Zr K and U L_3-edge EXAFS data for $(Zr_{0.8}U_{0.2})N$ and their corresponding Fourier transforms (FT) are shown in Fig. 2. The positions of all FT peaks shift to larger distances with increasing x in the $(Zr_{1-x}U_x)N$ compounds. The derived interatomic distances of the first four coordination shells (N_1, Me_1, Me_2, and Me_3) around Zr and U atoms are plotted in Fig. 3 together with the lattice parameter of the $(Zr_{1-x}U_x)N$ samples. For comparison,

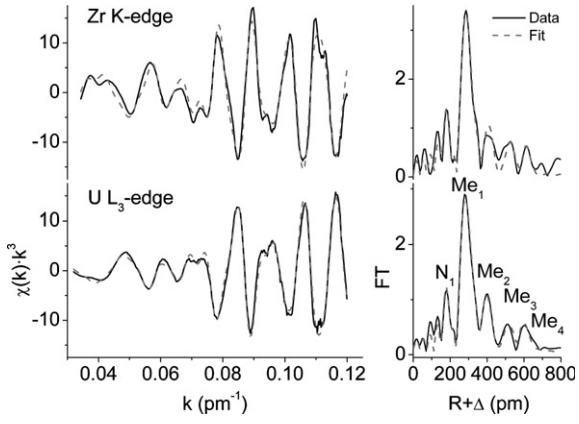

Fig. 2. Zr K-edge (top) and U L_3-edge (bottom) EXAFS spectra of $(Zr_{0.8}U_{0.2})N$ solid solution.

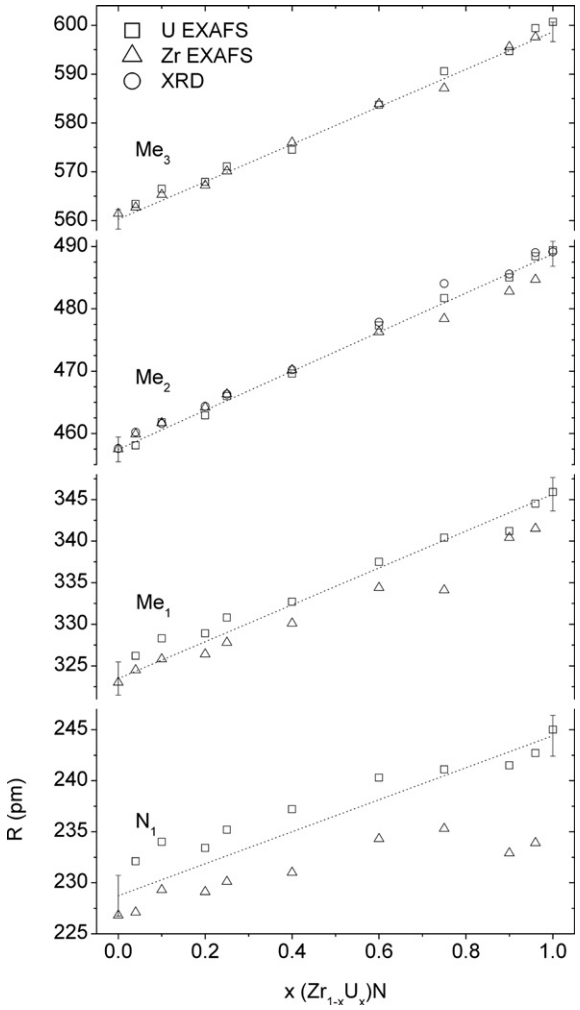

Fig. 3. Interatomic distances of N_1, Me_1, Me_2 and Me_3 coordination shells around U and Zr atoms in $(Zr_{1-x}U_x)N$ as determined by EXAFS spectroscopy. The ΔR error bars at $x = 0$ and 1 are ±0.02 Å. The lattice parameter obtained by X-ray diffraction is shown for comparison. The Vegard lines for the interatomic distances are derived from XRD data of Ref. [2,3].

Vegard lines corresponding to the individual shell distances derived from the XRD data of Ref. [2,3] are also shown. The Me_2 and Me_3 atoms around Zr and U are generally at the same distance as determined from the crystallographic values. This indicates the formation of a homogenous solid solution without any cluster formation, since both the Me_2 and Me_3 atomic positions are located in the neighbouring unit cells, representing the bulk crystal structure as probed by X-ray diffraction.

In contrast to the more distant Me_2 and Me_3 atoms, the N_1 and Me_1 coordination shells represent the immediate local structure around Zr and U atoms. The U–N and U–Me_1 interatomic distances follow the Vegard behaviour for all $(Zr_{1-x}U_x)N$ compositions. The local structure around Zr shows a different behaviour. The Zr–N bond distance at low x (high Zr) increases with x. At $x > 0.6$ in $(Zr_{1-x}U_x)N$, however, the Zr–N distance ceases to increase and remains relatively constant at 232–235 pm.

The Zr–Me_1 distance determined by EXAFS, and the distance expected from the crystal structure, also differ slightly with rising x. The obtained Zr/U ratios of the Me_1 shell are close to the corresponding composition of $(Zr_{1-x}U_x)N$, indicating that no clusters enriched in Zr or U are formed. The disorder, σ^2, around the U and Zr atoms is similar (σ^2(U–N) = 0.006(2), σ^2(U–Me_1 = 0.004(1), σ^2 (Zr–N) = 0.005(2), σ^2(Zr–Me_1 = 0.005(1) × 10^4 pm^2). The disorder remains nearly constant with composition x, again indicating that there is no significant change in the local Zr/N and U/N ratio within the $(Zr_{1-x}U_x)N$ samples.

4. Discussion

The U–N and Zr–N bond lengths obtained for $(Zr_{1-x}U_x)N$ clearly show that U accommodates the contraction of its local environment with increasing Zr content. Zr adapts to the unit cell expansion induced by higher U contents up to an U content of $x < 0.6$, whereas at $x > 0.6$ the immediate coordination environment around Zr is contracted compared to the bulk structure.

Similar EXAFS observations are reported in the isostructural (NaCl-type) LaS–US solid solution [10]. The U–S bond distance follows the Vegard law completely, whereas the La–S bond distance is almost independent of the U content for low U contents, but varies linearly at higher U content. Also in the more ionic oxides, U is generally able to accommodate a change of its local coordination environment [8,9]. In contrast, the Zr–O bond length in cubic stabilized zirconia, such as $(Zr,Y)O_{2-x}$ or $(Zr,Yb)O_{2-x}$, does not depend on the Y or Yb content and remains constant at 210–217 pm, similar to the pure oxide ZrO_2 [16,17]. The different behaviour of Zr and U ions in accommodating lattice expansion or contraction is related to their electronic structure. The U^{4+} ion has two more valence electrons than the Zr^{4+} ion with a closed [Kr] shell, which can contribute to bonding and allow flexibility in the U–O bond length. In the nitrides, their metallic bonding character enables the Zr–N interatomic distance to vary at low and intermediate U content, so that the local structure is homogeneous in the composition range of transmutation fuels. However, the limited ability of Zr to expand its Zr–N bond length at higher U (actinide) content seems to be one key parameter restricting the formation of nitride solid solutions between Zr and actinides larger than U, as has been observed for ZrN–ThN [4] and ZrN–AmN [7].

5. Conclusion

Solid solutions of ZrN and UN were prepared for EXAFS measurements by a sol–gel route combined with infiltration and carbothermic reduction in the presence of carbon in a nitrogen gas stream at 1600 °C. The lattice parameter, and the distances determined by EXAFS for the coordination shells Me_2 (460–490 pm) and Me_3 (560–600 pm) around Zr and U atoms all follow the Vegard law. The U–N distance also follows the Vegard law. In contrast, the Zr–N bond distance increases with lattice parameter until $x = 0.6$, but remains constant at 232–235 pm for $x > 0.6$. This indicates that the material is homogeneous at the local atomic scale in the composition range of transmutation fuel, but it is heterogeneous in the uranium-rich part of the ZrN–UN solid solution.

Acknowledgements

We would like to acknowledge the assistance of A. Accarier, M. Holzhäuser and C. Boshoven in the preparation of samples, and thank the *ANKA Angstroemquelle Karlsruhe* for providing beamtime for the EXAFS measurements.

References

[1] M. Burghartz, G. Ledergerber, H. Hein, R.R. van der Laan, R.J.M. Konings, J. Nucl. Mater. 288 (2001) 233.
[2] T.W. Baker, Acta Crystallogr. 11 (1958) 300.
[3] E.H.P. Cordfunke, J. Nucl. Mater. 56 (1975) 319.
[4] H. Holleck, in: A.J. Freeman, C. Keller (Eds.), The Constitution of Ternary Actinide–Transition Metal–Carbon and Actinide–Transition Metal–Nitrogen Systems, Handbook on the Physics and Chemistry of the Actinides, vol. 4, North Holland, Amsterdam, 1986, p. 209.
[5] H. Holleck, E. Smailos, F. Thümmler, Monatshefte für Chemie 99 (1968) 985.
[6] Y. Arai, K. Nakajima, J. Nucl. Mater. 281 (2000) 244.
[7] K. Minato, M. Akabori, M. Takano, Y. Arai, K. Nakajima, A. Itoh, T. Ogawa, J. Nucl. Mater. 320 (2003) 18.
[8] P. Martin, M. Ripert, Z. Petit, T. Reich, C. Hennig, F. D'Acapito, J.L. Hazemann, O. Proux, J. Nucl. Mater. 312 (2003) 103.
[9] J. Purans, G. Heisbourg, N. Dacheux, Ph. Moisy, S. Hubert, Phys. Scr. T115 (2005) 925.
[10] A. Bombardi, F. d'Acapito, K. Mattenberger, O. Vogt, G.H. Lander, Phys. Rev. B 68 (2003) 104414.
[11] A. Fernández, D. Haas, R.J. Konings, J. Somers, J. Am. Ceram. Soc. 85 (2002) 694.
[12] G. Ledergerber, Z. Kopajtic, F. Ingold, R.W. Stratton, J. Nucl. Mater. 188 (1992) 28.
[13] M.A. Denecke, J. Rothe, K. Dardenne, H. Blank, J. Hormes, Phys. Scr. T 115 (2005) 1001. <http://ankaweb.fzk.de>.
[14] G.N. George, I.J. Pickering, EXAFSPAK: A Suite of Computer Programs for Analysis of X-ray Absorption Spectra, Standford Synchrotron Radiation Laboratory, Stanford, 1995.
[15] A.L. Ankudinov, B. Ravel, J.J. Rehr, S.D. Conradson, Phys. Rev. B 58 (1998) 7565.
[16] M.H. Tuilier, J. Dexpert-Ghys, H. Dexpert, P. Lagarde, J. Solid State Chem. 69 (1987) 153.
[17] D. Komyoji, A. Yoshiasa, T. Moriga, S. Emura, F. Kanamaru, K. Koto, Solid State Ionics 50 (1992) 291.